Test of Full and Partial Tube Dilation Pictures in Entangled Blends of Linear Polyisoprenes

Hiroshi Watanabe,* Satoshi Ishida, Yumi Matsumiya, and Tadashi Inoue

Institute for Chemical Research, Kyoto University, Uji, Kyoto 611-0011 Japan

Received March 4, 2004; Revised Manuscript Received June 10, 2004

ABSTRACT: The molecular picture of dynamic tube dilation (DTD) was tested for viscoelastic and dielectric data for two series of entangled binary blends of linear *cis*-polyisoprenes (PI) having $10^{-3}M_2 =$ 308 and $10^{-3}M_1 = 94.0$ or 21.4. The volume fraction v_2 of the high-M chains was varied from 0.005 to 0.5. The Struglinski−Graessley parameter r_{SG} ($= M_2M_e^2M_1^{-3}$), specifying the constraint release (CR) contribution to the relaxation of high-M chains at small v_2, was quite different for the two series of blends ($r_{SG} = 0.0093$ and 0.79). For large v_2 ($= 0.5$), the full-DTD picture treating the relaxed portions of the chains as a simple solvent held satisfactorily in the entire range of time t irrespective of the r_{SG} value. However, on a decrease of v_2, this picture began to fail at intermediate t and further at long t (in the terminal regime of the high-M chains), and the failure was more significant for the blend with small r_{SG}. This failure occurred when the number $\beta_{CR}(t)$ of the entanglement segments equilibrated through the Rouse−CR dynamics was smaller than the equilibration number assumed in the full-DTD picture, $\beta_{f-DTD}(t) = \{\varphi'(t)\}^{-d}$ with $\varphi'(t)$ and d ($= 1.3$) being the dielectrically determined tube survival fraction and the dilation exponent, respectively. A test was made also for the partial-DTD picture incorporating the maximum number of the segments that can be CR-equilibrated under the given $\varphi'(t)$ value. The behavior of the blends of various v_2, including the low-v_2 limit, was considerably well described by the partial-DTD picture, although nonnegligible differences still remained between this picture and experiments. Thus, the partial-DTD picture (including the full-DTD picture as an extreme case) was quite tempting, and a brief discussion was made for a possible improvement of existing molecular models on the basis of this molecular picture.

1. Introduction

The key concept in the entanglement dynamics is the time-dependent changes in the topological constraint for a given chain (probe) due to motion of the surrounding chains (matrix).[1,2] These changes activate the motion of the probe chain in a direction lateral to its backbone and induces viscoelastic relaxation. The current tube model describes this relaxation as a result of the tube motion occurring through the *constraint release* (CR)[1−4] or *dynamic tube dilation* (DTD)[5−11] mechanism, the latter intimately related to the double reptation mechanism.[12−14]

In the CR molecular picture, the entanglement segment of the molecular weight M_e and a size a is utilized as the motional unit of the probe chain and the local CR jumps of respective segments (activated by the matrix motion) are accumulated to induce larger scale motion of the probe. This CR motion competes with the longitudinal motion of the probe along the tube to determine the viscoelastic relaxation time/mode distribution of the probe. Thus, a molecular description of this combined relaxation process requires full analysis of the motion of individual entanglement segments occurring through several mechanisms.[1,2,4]

In contrast, the DTD molecular picture assumes that successive $\beta(t)$ entanglement segments are mutually equilibrated through their CR motion in a *given* time scale t to become a larger, coarse-grained motional unit of a size $a'(t) = a\{\beta(t)\}^{1/2}$. This equilibration results in a decay of the stress by a factor of $1/\beta(t)$.[1,2,5] In the DTD picture, $\beta(t)$ is usually taken to be the maximum number of the entanglement segments that can be CR-equilibrated in the given t. Then, the coarse-grained motional unit has no freedom to exhibit lateral CR motion, and the probe chain is modeled to relax simply through the longitudinal motion along a dilated tube of the diameter $a'(t)$. This molecular picture neglects the Rouse-like mode distribution of the CR-induced stress decay but enables much *simpler* analysis/formulation of the relaxation function (compared to the full analysis in the CR picture). Thus, the DTD picture is tempting if this neglect of the CR-mode distribution raises no severe problem.

Furthermore, the DTD model frequently assumes that relaxed portions of the chains in the system give no effective topological constraint and are equivalent to a solvent.[5−8] Under this assumption, the number β of the CR-equilibrated segments and the dilated tube diameter a' are related to a fraction of the nonrelaxed portion of the chains φ' (= survival fraction of the dilated tube) as

$$\beta(t) = \{\varphi'(t)\}^{-d}, \quad a'(t) = a\,\{\varphi'(t)\}^{-d/2} \tag{1}$$

Here, d ($= 1-1.3$) is the dilation exponent. The β and a' values specified by eq 1 are the maximum values expected from a given φ' value, meaning that the model assumes the *full dilation* of the tube. This assumption is justified if the CR-equilibration over the $\{\varphi'(t)\}^{-d}$ entanglement segments can actually occur in the given time scale t. (In our previous papers,[15−21] the full-DTD was simply referred to as DTD. In this paper, we utilize the term "full-DTD" in order to distinguish it from "partial-DTD" explained later.)

Recently, we tested this molecular picture of full-DTD for blends of linear *cis*-polyisoprene (PI) chains.[21] The PI chains have the type-A dipoles parallel along the

* To whom correspondence should be addressed.

10.1021/ma0495689 CCC: $27.50
Published on Web 07/29/2004

Table 1. Characteristics of Linear PI Samples

code	$10^{-3}M_w$	M_w/M_n
L308	308	1.08
L94	94.0	1.05

backbone and their dielectric relaxation detects the end-to-end vector fluctuation.[19] No dielectric relaxation is activated by the DTD mechanism itself except a contribution from the chain fluctuation in the dilated tube edge, and the dielectric relaxation function of the blends $\Phi(t)$ is essentially equivalent to the tube survival fraction $\varphi'(t)$.[15,16,19,21] In contrast, the viscoelastic relaxation is induced by the DTD mechanism and the corresponding relaxation function for the case of full-DTD is expressed as $\mu(t) = \{\varphi'(t)\}^{1+d}$. Then, the $\mu(t)$ and $\Phi(t)$ data should satisfy the relationship[15,16,19,21]

$$\mu_{f-DTD}(t) = \{\Phi(t)\}^{1+d} + \text{tube-edge contribution (for full-DTD)} \quad (2)$$

In the PI/PI blends examined in our recent work,[21] the low-M and high-M chains had widely separated molecular weights, $M_1 \cong 4M_e$ and $M_2 \cong 61M_e$ ($M_e = 5.0 \times 10^3$), and the volume fraction v_2 of the high-M chain was varied from 0.005 to 0.5. In these blends, the Struglinski−Graessley parameter[22] specifying the CR contribution to the relaxation of the high-M chains at $v_2 \to 0$, $r_{SG} = M_2M_e^2M_1^{-3} = 0.79$, was larger than the threshold value ($\cong 0.5$)[1] for the CR dominance. Indeed, the Rouse-like CR relaxation was confirmed for the dilute high-M chains with $v_2 \leq 0.01$. At larger v_2 (≥ 0.05) where high-M chains themselves were mutually entangled, comparison of the dielectric and viscoelastic data revealed that the full-DTD relationship (eq 2 with an experimentally determined value of $d \cong 1.3$) holds at short and long t where the low-M and high-M chains exhibit respective terminal relaxation but fails at intermediate t where the CR-equilibration occurred only insufficiently (over β entanglement segments with $\beta < \{\varphi'(t)\}^{-d}$; cf. eq 1).[21]

This failure of the full-DTD picture is intimately related to the CR-equilibration rate. It is of interest to test this picture also for blends having a smaller r_{SG} value and exhibiting slower CR-equilibration compared to the previously examined blends. We have made this test for PI/PI blends with $M_1 \cong 19M_e$ and $M_2 \cong 61M_e$ ($r_{SG} = 0.0093$). It turned out that the full-DTD relationship between μ and Φ (eq 2) failed more severely for these blends than for the previous blends ($r_{SG} = 0.79$) because of the insufficient CR-equilibration at intermediate to long t. Furthermore, the μ and Φ data of the two series of the blends were found to be much better described by a partial-DTD relationship accounting for this insufficient equilibration through the Rouse−CR mechanism. This paper presents details of these results.

2. Experimental Section

Previously synthesized/characterized linear *cis*-polyisoprene (PI) samples[15,18] were used. Molecular characteristics of these samples are summarized in Table 1. The sample code number indicates the molecular weight in unit of 1000.

The systems subjected to viscoelastic and dielectric measurements were blends of high-M and low-M PI samples (L308 and L94) having various values of the L308 volume fraction v_2. The blends were prepared by dissolving prescribed masses of L308 and L94 in benzene at $\cong$ 5 wt % and then allowing benzene to thoroughly evaporate.

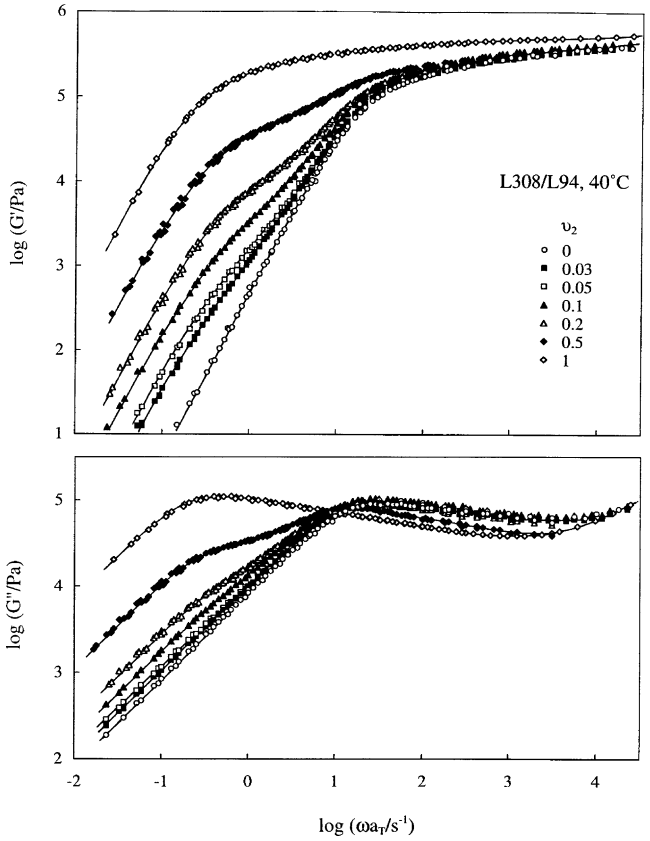

Figure 1. Storage and loss moduli G' and G'' of the L308/L94 blends at 40 °C. Solid curves are guide for eye.

For these L308/L94 blends, dynamic viscoelastic measurements were conducted at several temperatures (T/°C = −20, −10, 0, 10, 25, 40, 50, 60, 70, and 80) with a laboratory rheometer (ARES; Rheometrics) to determine the storage and loss moduli $G'(\omega)$ and $G''(\omega)$ at various angular frequencies ω. A parallel plate fixture of a diameter of 25 mm was used. The amplitude of oscillatory strain was kept small to ensure the linearity of the viscoelastic response.

Dielectric measurements were conducted for the blends charged in a guarded parallel-plate dielectric cell (of a vacant capacitance of 120 pF) with a transformer bridge (1620A, QuadTech) and a previously made circuit,[18] the latter being comprising of a function generator (WF1944, NF Corp.), an electrometer (TR8411, Advantest), and a digital recorder (DL708G, Yokogawa). The bridge was used for high-ω measurements (at T = 10, 25, 40, 50, 60, 70, and 80 °C) with the usual current-compensation method,[23] and the circuit was utilized for long-time measurements (at T = 40 °C) with the adsorption current method. Details of the latter method were described elsewhere.[18]

The time−temperature superposition held excellently for both viscoelastic and dielectric data with the same shift factor a_T. These data were reduced/compared at 40 °C.

3. Results

3.1. Overview of Viscoelastic and Dielectric Data. For the L308/L94 blends of various L308 content v_2, Figure 1 shows dependence of the storage and loss moduli $G'(\omega)$ and $G''(\omega)$ at 40 °C on the angular frequency ω. The dielectric loss $\epsilon''(\omega)$ and a decrease of the dynamic dielectric constant $\epsilon_0 - \epsilon'(\omega)$ (ϵ_0 = static dielectric constant) are shown in Figure 2. The Struglinski−Graessley parameter for those blends, $r_{SG} = M_2M_e^2M_1^{-3} = 0.0093$, is much smaller than the threshold value ($\cong 0.5$)[1], and no CR-dominance is expected for the terminal relaxation of the high-M chain at $v_2 \to 0$.

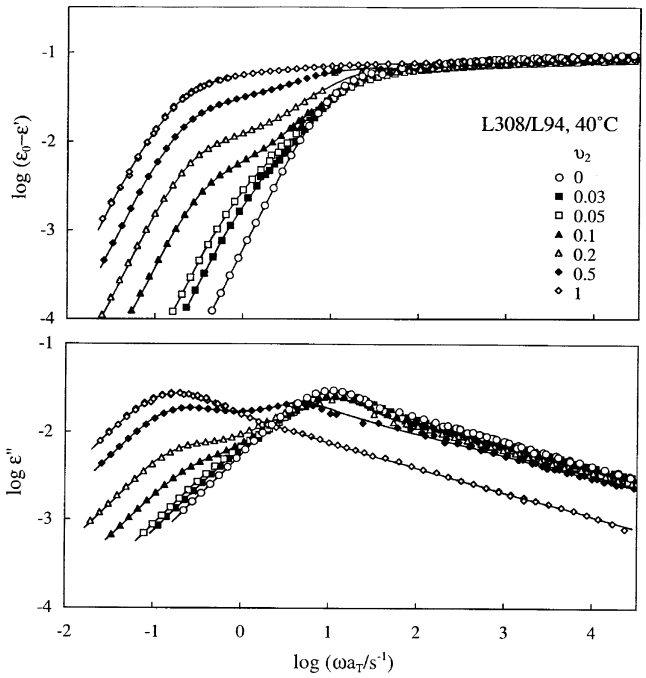

Figure 2. Decrease of dynamic dielectric constant, $\epsilon_0-\epsilon'$, and dielectric loss, ϵ'', of the L308/L94 blends at 40 °C. The dielectric relaxation function $\Phi(t) = v_1\Phi_1(t) + v_2\Phi_2(t)$ was evaluated from the ϵ'' data with the previously reported method.[21] Solid curves indicate $\epsilon_0 - \epsilon'$ and ϵ'' recalculated from this $\Phi(t)$.

In Figure 1, we clearly observe two-step viscoelastic relaxation similar to that of extensively investigated polystyrene blends.[1] The fast relaxation seen at $\omega \cong 10$ s^{-1} is attributed to the full (terminal) relaxation of the low-*M* chain (L94) and partial relaxation of the high-*M* chain (L308), while the slow relaxation at $\omega < 1$ s^{-1} is attributed to the full relaxation of the high-*M* chain. Similar two-step relaxation is noted for the dielectric data in the same range of ω (Figure 2), confirming that the global motion of the high-*M* and low-*M* PI chains is dielectrically active because of their type-A dipoles. (The PI chains also have the type-B dipoles perpendicular to their backbone. However, the dielectric relaxation due to these dipoles reflects local motion of monomeric segments[19] and emerges at high ω not covered in our experiments.)

Despite this similarity, we also note an important difference between the viscoelastic and dielectric data. At low $\omega < 1$ s^{-1}, a decrease of the viscoelastic loss G'' on a decrease of v_2 to 0.2 (Figure 1) is much larger than the corresponding decrease of the dielectric loss ϵ'' (Figure 2). This difference reflects an intrinsic difference between the viscoelastic and dielectric relaxation: The viscoelastic relaxation reflects an *isochronal* orientation anisotropy of individual segments and is activated by the DTD mechanism, while the dielectric relaxation detects orientational correlation of these segments at two *separate* times 0 and *t* and is insensitive to this mechanism.[1,15,19−21] Indeed, this difference enables us to test the DTD picture through comparison of the viscoelastic and dielectric data.

3.2. Evaluation of Terminal Viscoelastic and Dielectric Parameters. In the L308/L94 blends with small v_2 ($\leq$ 0.1), the relaxation behavior of the low-*M* chains is negligibly affected by the high-*M* chains; see the high-ω relaxation behavior in Figures 1 and 2. For this case, viscoelastic parameters characterizing the terminal relaxation of the high-*M* chains in the blends are simply obtained by subtracting the data of the monodisperse low-*M* chain system from the blend data after correction for the low-*M* chain content in the blend. For example, the zero-shear viscosity $\eta_{2,B}$, the elastic coefficient $A_{2,B}$, and the steady-state compliance $J_{2,B}$ of the high-*M* chains in the blend are obtained as[1,21,24,25]

$$\eta_{2,B} = \eta_B - (1 - v_2)\eta_{1,m}, \quad A_{2,B} = A_B - (1 - v_2)A_{1,m}, \quad J_{2,B} = A_{2,B}/(\eta_{2,B})^2 \quad (3)$$

Here, the subscripts "B" and '1,m' stand for the data of the blend and monodisperse system of the low-*M* chains, respectively. The terminal viscoelastic relaxation time of the high-*M* chain in the blend, defined as the second-moment average relaxation time, is given by[1,26,27]

$$\langle\tau_{2,B}\rangle_G = J_{2,B}\eta_{2,B} \quad (4)$$

The viscosity η_B and compliance J_B ($=A_B/\eta_B^2$) of the blends utilized for evaluation of the above terminal parameters are summarized in Table 2.

Similarly, the terminal dielectric relaxation time of the high-*M* chain in the blend is evaluated from the ϵ'' and $\Delta\epsilon' = \epsilon_0 - \epsilon'$ data of the blend and the monodisperse low-*M* chain system as[18,19]

$$\langle\tau_{2,B}\rangle_\epsilon = \frac{\left[\frac{1}{\omega^2}\{\Delta\epsilon_B'(\omega) - (1 - v_2)\Delta\epsilon_{1,m}'(\omega)\}\right]_{\omega\to 0}}{\left[\frac{1}{\omega}\{\epsilon_B''(\omega) - (1 - v_2)\epsilon_{1,m}''(\omega)\}\right]_{\omega\to 0}} \quad (5)$$

(The expression of ϵ'' and $\Delta\epsilon'$ in terms of the dielectric spectrum is formally identical to the expression of G'' and G' in terms of the viscoelastic spectrum,[19] thereby enabling us to utilize eq 5 for evaluation of the terminal dielectric relaxation time.)

In blends with large $v_2 > 0.1$, the relaxation of the low-*M* chains is moderately retarded by the concentrated high-*M* chains, as noted from the shift of the high-ω peaks of ϵ'' and G'' in Figures 1 and 2. In principle, this retardation effect is to be considered in the evaluation of the terminal parameters of the high-*M* chains. However, for large v_2, the low-*M* chains hardly contributed to the blend data at *low* ω and the values

Table 2. Viscosity η_B and Compliance J_B of PI/PI Blends at 40 °C

v_2	$\log(\eta_B/\text{Pa s})$	$\log(J_B/\text{Pa}^{-1})$
	L308/L94 Blends	
0 (L94)	3.92	−5.10
0.03	4.03	−4.50
0.05	4.09	−4.44
0.1	4.25	−4.31
0.2	4.47	−4.29
0.5	5.05	−4.56
1 (L308)	5.81	−5.25
	L308/L21 Blends[a]	
0 (L21)	1.72	−5.51
0.005	1.77	−3.80
0.01	1.83	−3.52
0.02	1.93	−3.26
0.03	2.10	−3.13
0.05	2.33	−3.11
0.1	2.87	−3.24
0.2	3.73	−3.78
0.5	4.85	−4.51
1 (L308)	5.81	−5.25

[a] Examined in previous study.[21]

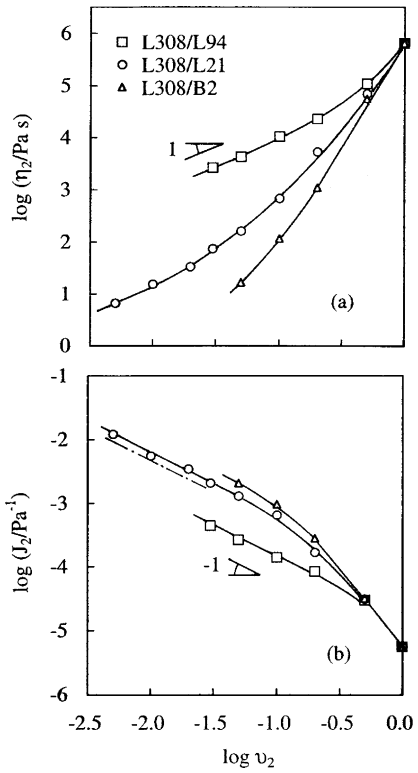

Figure 3. Viscosity $\eta_{2,B}$ and compliance $J_{2,B}$ of the high-M chain (L308) in the L308/L94 and L308/L21 blends at 40 °C. For comparison, $\eta_{2,sol}$ and $J_{2,sol}$ of the same high-M chain in the L308/B2 solutions (in the isofriction state) are also shown. The dash−dot line in part b shows the compliance for the Rouse−CR mechanism, $J_{Rouse} = 2M_2/5c_2RT$.

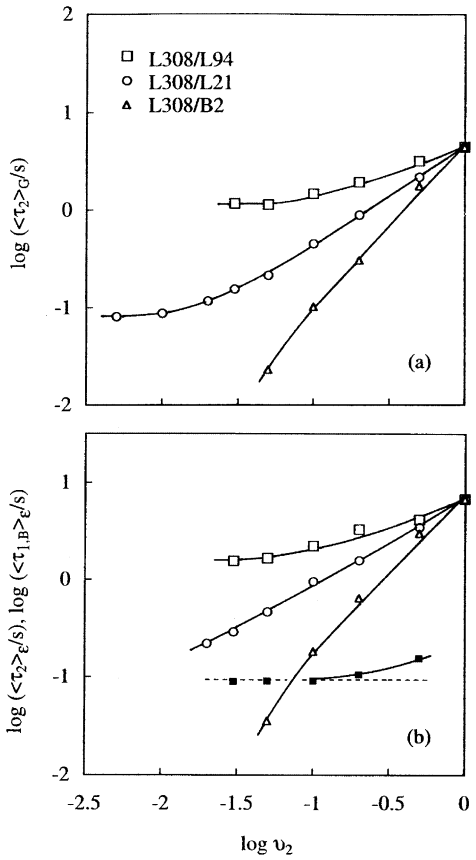

Figure 4. Viscoelastic and dielectric terminal relaxation times $\langle\tau_{2,B}\rangle_G$ and $\langle\tau_{2,B}\rangle_\epsilon$ of the high-M chain (L308) in the L308/L94 and L308/L21 blends at 40 °C. For comparison, $\langle\tau_{2,sol}\rangle_G$ and $\langle\tau_{2,sol}\rangle_\epsilon$ of the same high-M chain in the L308/B2 solutions[21] (in the iso-friction state) are also shown. In part b, the filled squares denote the dielectric terminal relaxation time $\langle\tau_{1,B}\rangle_\epsilon$ of the low-M chain (L94) in the L308/L94 blends at 40 °C, and the horizontal dotted line shows the dielectric $\langle\tau_{1,m}\rangle_\epsilon$ of the same low-M chain in its monodisperse system at 40 °C.

of these parameters were quite insensitive to that effect. For this reason, we utilized eqs 3−5 to evaluate the terminal parameters in the entire range of υ_2.

The $\langle\tau_{2,B}\rangle_\epsilon$ obtained from eq 5 agreed with a relaxation time $1/\omega_{p,low}$ evaluated from the angular frequency $\omega_{p,low}$ of the low-ω ϵ'' peak for the high-M chain (Figure 2). This agreement results from a narrow distribution of the dielectric modes being reflected in the sharp ϵ'' peak.[19] Since the low-M chain exhibits a similarly sharp ϵ'' peak at high ω (Figure 2), we evaluated its terminal dielectric relaxation time $\langle\tau_{1,B}\rangle_\epsilon = 1/\omega_{p,high}$ from the frequency $\omega_{p,high}$ of this peak.

3.3. υ_2 Dependencies of Terminal Parameters of High-M Chain. Figures 3 and 4 show υ_2 dependencies of the terminal parameters $\eta_{2,B}$, $J_{2,B}$, $\langle\tau_{2,B}\rangle_G$, and $\langle\tau_{2,B}\rangle_\epsilon$ of the high-M chain in the L308/L94 blends (unfilled squares). For comparison, the dielectric $\langle\tau_{1,m}\rangle_\epsilon$ and $\langle\tau_{1,B}\rangle_\epsilon$ of the low-M chain in its monodisperse system and the blends are shown in Figure 4b with the horizontal dotted line and filled squares, respectively. In the previous study,[21] the relaxation of the same high-M chain (L308) was examined in blends with much shorter matrix PI chains (L21; $M_1 = 21.4 \times 10^3 \cong 4M_e$, $M_w/M_n = 1.04$) and in solutions in a nonentangling marginal solvent, an oligometric vinyl-rich butadiene (B2; $M \cong 2 \times 10^3$, $M_w/M_n \cong 2$). The terminal parameters of the high-M chain in these blends and solutions, reduced at the isofriction state[21] (at 40 °C for the blends), are also shown in Figures 3 and 4 (circles and triangles). In all systems, the dielectric $\langle\tau_{2,B}\rangle_\epsilon$ is a little longer than the viscoelastic $\langle\tau_{2,B}\rangle_G$ (because of the difference between the dielectric and viscoelastic relaxation explained earlier) but their υ_2 dependencies are quite similar to each other (cf. Figure 4, parts a and b), confirming that the slow dielectric relaxation detects the global motion of the high-M chain.

In the L308/L21 and L308/94 blends, the relaxation behavior of the high-M L308 chain significantly changes with the length of the entangling matrix chains. To examine this change, we first summarize the behavior in the short L21 matrix fully analyzed in the previous study. The terminal viscoelastic mode distribution of the L308 chain, reflected in the J_2 data (Figure 3b), is almost indistinguishable in the L21 matrix and nonentangling solvent B2. Furthermore, for $\upsilon_2 \leq 0.01$, the L308 chains in the L21 matrix behaves as dilute chains to exhibit characteristic relationships $J_{2,B} \propto \upsilon_2^{-1}$, $\eta_{2,B} \propto \upsilon_2$, and $\langle\tau_{2,B}\rangle_G \propto \upsilon_2^0$ (cf. Figures 3 and 4a), and the $J_{2,B}$ data are numerically close to the Rouse−CR value shown with the dash−dot line in Figure 3b, $J_{Rouse} = 2M_2/5c_2RT$ with c_2 and R being the high-M chain concentration (in mass/volume unit) and the gas constant, respectively. These results indicate that the entanglement for the L308 chain due to the short L21 chains becomes ineffective at long t through the Rouse-like CR mechanism, which is in harmony with the large value of the Struglinski−Graessley parameter for the L308/L21 blends, $r_{SG} = 0.79$. Thus, the measured $\langle\tau_{2,B}\rangle_G$ of the dilute L308 chain ($\upsilon_2 \leq 0.01$) can be utilized as the terminal viscoelastic CR time (defined as the second-moment average relaxation time)[27]

$$\tau_{CR,G}^{\circ} = 0.08 \text{ s for dilute L308 in L21 matrix} \quad (6)$$

In the entire range of v_2, the L308 relaxation in the L308/L21 blends is affected by the CR mechanism and cannot be completed at $t < \tau_{CR,G}^{\circ}$. In contrast, the relaxation in the solvent B2 is free from the CR effect of B2 and can be completed even at $t \ll \tau_{CR,G}^{\circ}$. For this reason, $\langle\tau_2\rangle$ of L308 is different in the L21 matrix and B2 at small v_2; see Figure 4. Except for this CR effect in L21 fully discussed in the previous paper,[21] the terminal relaxation behavior of the L308 chains is similar in the entangling L21 matrix and the nonentangling solvent B2, as most clearly noted from the close coincidence of J_2 in these environments (cf. Figure 3b).

Now, we focus on the relaxation of L308 in the L94 matrix. Figures 3 and 4 clearly demonstrate that $\eta_{2,B}$, $\langle\tau_{2,B}\rangle_G$, and $\langle\tau_{2,B}\rangle_\epsilon$ of L308 are larger in the L94 matrix than in the shorter L21 matrix and $J_{2,B}$ is smaller in the L94 matrix. Correspondingly, the v_2 dependencies of these terminal parameters are considerably weaker in the L94 matrix. Furthermore, for $v_2 \leq 0.2$, $J_{2,B}$ in the L94 matrix is considerably smaller than $J_{2,sol}$ in the solvent B2, meaning that the terminal viscoelastic relaxation intensity of L308 is larger in this matrix and the similarity with the solution vanishes. These features, similar to those observed for PS/PS blends[1] with small r_{SG}, indicate that the CR relaxation due to the matrix chain motion is suppressed in the L308/L94 blend.

This suppression of the CR relaxation can be quantified from the terminal viscoelastic CR relaxation time $\tau_{CR,G}^{\circ}$ expected for the dilute L308 chain in the L94 matrix. Applying the Rouse−CR relationship, $\tau_{CR,G}^{\circ} \propto M_1^3 M_2^2 M_e^{-3}$ (confirmed for dilute probe PS chains entangled with much shorter matrix PS chains[1]), to the $\tau_{CR,G}^{\circ}$ data of L308 in the L21 matrix (eq 6), we obtain an estimate, $\tau_{CR,G}^{\circ} \cong 7$ s in the L94 matrix. The $\langle\tau_{2,B}\rangle_G$ and $\langle\tau_{2,B}\rangle_\epsilon$ values in the L94 matrix (Figure 4) are significantly smaller than this estimate, indicating that the L308 chain in this matrix relaxes before the CR-equilibration due to the matrix chain motion occurs to the maximum level.[28] This result is in harmony with the small r_{SG} value (= 0.0093) of the L308/L94 blends.

This suppression of the CR-equilibration *below the maximum level* does not mean that the CR mechanism hardy contributes to the actual relaxation of the L308 chain in the L94 matrix. Instead, the local CR jumps of respective entanglement segments of the L308 chain undoubtedly occur at $t \cong \langle\tau_{1,B}\rangle_\epsilon$ ($\ll \langle\tau_{2,B}\rangle$) where the matrix chains exhibit their terminal relaxation. Fast CR modes activated by these jumps significantly contribute to the actual relaxation of the L308 chain in the L94 matrix and play an important role in the molecular picture of the dynamic tube dilation, as explained later in more details.

4. Discussion

4.1. Test of Full-DTD Picture. The key quantities in the molecular picture of dynamic tube dilation (DTD) for binary blends are the survival fractions of the dilated tubes for the low-M and high-M chains, $\varphi_1'(t)$ and $\varphi_2'(t)$, and the average survival fraction given by[1,5]

$$\varphi'(t) = (1 - v_2)\varphi_1'(t) + v_2\varphi_2'(t) \quad (7)$$

The full-DTD picture assumes that the relaxed portions of the high-M and low-M chains behave as a simple solvent to determine the dilated tube diameter $a'(t)$ and this diameter is the same for these chains.[1,2,5−10] Under this assumption, $a'(t)$ is related to the nondilated tube diameter a as $a'(t) = a\{\varphi'(t)\}^{-d/2}$ with d being the dilation exponent. For the L308/L21 blends having $M_2 \gg M_1$, our previous study[21] showed that the dilation exponent d directly evaluated from the viscoelastic data of PI/PI blends and PI solutions at low ω is close to 1.3 and that the full DTD picture with this d value is valid at long t if v_2 is sufficiently large and the high-M chains are mutually entangled. (This d value is close to the theoretical prediction by Colby and Rubinstein[29] and the experimental value reported by Park and Larson.[30])

In this full-DTD picture, the normalized viscoelastic relaxation function $\mu(t)$ (=$G(t)/G_N$) is simply written as

$$\mu_{f-DTD}(t) = \{\varphi'(t)\}^{1+d}, \quad \text{with } d \cong 1.3 \text{ (for full-DTD)} \quad (8)$$

The tube survival fraction $\varphi'(t)$ appearing in eq 8 can be evaluated from the dielectric data of the PI/PI blends. If the chain fluctuation at the dilated tube edge is negligible, $\varphi'(t)$ coincides with the normalized dielectric relaxation function, $\Phi(t) = (1 - v_2)\Phi_1(t) + v_2\Phi_2(t)$ with the subscripts 1 and 2 standing for the low-M and high-M chains, respectively.[15,19−21] However, this fluctuation has a nontrivial contribution to $\Phi(t)$ of the blends unless v_2 is sufficiently large, as demonstrated previously.[18,20,21] For this case, the normalized dielectric relaxation functions $\Phi_j(t)$ of the low-M and the high-M chains ($j = 1$ and 2) are related to respective tube survival fractions $\varphi_j'(t)$ as[20,21]

$$\Phi_j(t) = \varphi_j'(t) - \frac{1}{4N_j}[\{a'(t)/a\} - 1]^2 = \varphi_j'(t) - \frac{1}{4N_j}[\{\varphi'(t)\}^{-d/2} - 1]^2 \quad (9)$$

Here, $N_j = M_j/M_e$ represents the number of (nondilated) entanglement segments per low-M and high-M chains ($j = 1$ and 2). Note that the $-[\{a'(t)/a\} - 1]^2/4N_j$ term represents the tube edge fluctuation effect on $\Phi_j(t)$ for an *arbitrary* value of the dilated diameter a' ($>a$),[20,21] and this term is replaced by $-[\{\varphi'(t)\}^{-d/2} - 1]^2/4N_j$ for the case of full-DTD.

Equations 7−9 specify the full-DTD relationship between the viscoelastic $\mu(t)$ and dielectric $\Phi(t)$ in the presence of the tube-edge fluctuation effect. This relationship can be tested for the $\mu(t)$ and $\Phi(t)$ data under a limitation that the concept of the dilated tube has a sound meaning and eq 9 is safely utilized only in a range of t where the dilated diameter $a'(t)$ is smaller than the chain size $aN_j^{1/2}$. Despite this limitation, $\varphi_j'(t)$ for the L308/L94 blends were successfully evaluated from the dielectric data (Figure 2) with a fitting method fully explained in our previous paper.[21]

We utilized the $\varphi_j'(t)$ thus evaluated to test the full-DTD relationship (with $d = 1.3$) for the L308/L94 blends in the range $v_2 \geq 0.1$ where the high-M chains are well entangled among themselves. The results are shown in Figure 5. For comparison, the previously obtained results for the L308/L21 blends[21] are shown in Figure 6. In both Figures 5 and 6, the circles show the $\mu(t)$ data obtained from the spectrum analysis[18] of the G' and G'' data, and the arrows indicate the terminal viscoelastic relaxation time $\langle\tau_{2,B}\rangle_G$ of the high-M chain. The dotted curves show $\mu_{f-DTD}(t)$ for the full-DTD process (eqs 7−9

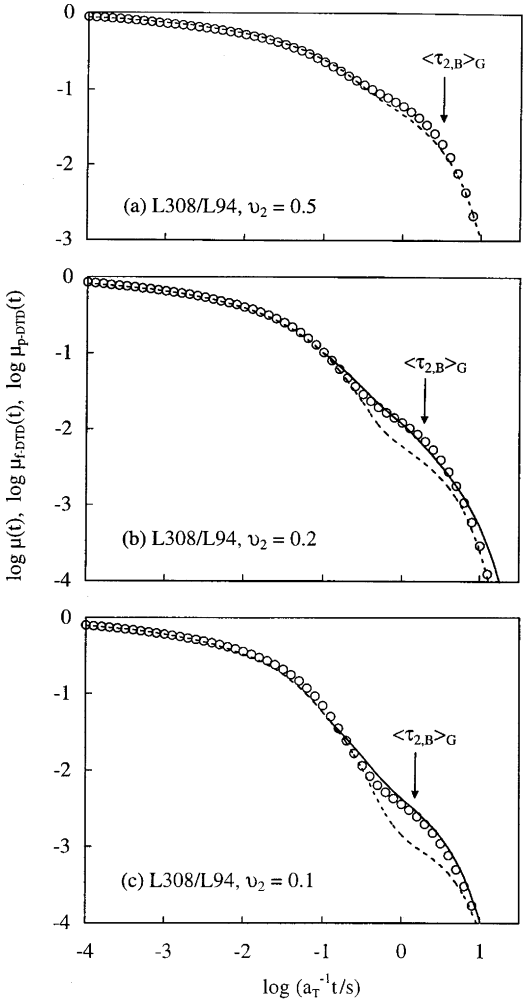

Figure 5. Comparison of the normalized viscoelastic relaxation function $\mu(t)$ (circles) of the L308/L94 blends ($\upsilon_2 = 0.5$, 0.2, and 0.1) with the relaxation functions $\mu_{f-DTD}(t)$ (dotted curves) and $\mu_{p-DTD}(t)$ (solid curves) calculated from the dielectric data on the basis of the full-DTD and partial-DTD pictures. $\mu_{p-DTD}(t)$ coincides with $\mu_{f-DTD}(t)$ in a range of t where the solid curves are not shown.

with $d = 1.3$) evaluated from the dielectric data, and the solid curves denote $\mu_{p-DTD}(t)$ for a partial-DTD process explained later. In Figure 5, the results for various υ_2 are shown in separate panels to avoid heavy overlapping of the data points and curves.

For the L308/L21 blends (Figure 6), the full-DTD relationship (dotted curves) satisfactorily describes the $\mu(t)$ data at short and long t where the low-M and high-M chains exhibit respective terminal relaxation. However, at intermediate t, this relationship underestimates $\mu(t)$ in particular for small υ_2 (= 0.1). This failure of the full-DTD picture indicates that the tube at intermediate t does not dilate to the diameter expected from this picture because of the insufficient CR-equilibration, as discussed previously.[21]

For the L308/L94 blends (Figure 5), we note a qualitatively similar failure of the full-DTD picture. Quantitatively, the failure is severer for these blends: For example, for $\upsilon_2 = 0.1$, the full-DTD curve agrees well with the $\mu(t)$ data for the L308/L21 blend at $\langle\tau_{2,B}\rangle_G/3 < t < \langle\tau_{2,B}\rangle_G$ in the terminal regime (Figure 6) while no agreement is observed for the L308/L94 blend in this regime (Figure 5c). This result suggests that the CR-equilibration is more difficult to occur in the L308/L94 blend than in the L308/L21 blend, as expected from their r_{SG} values (= 0.0093 and 0.79).

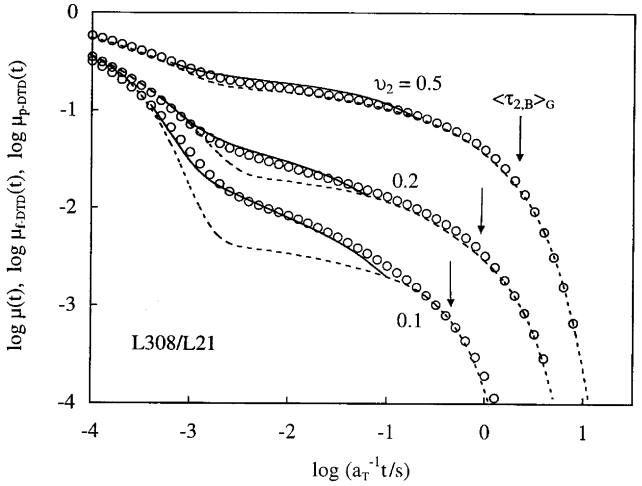

Figure 6. Comparison of the normalized viscoelastic relaxation function $\mu(t)$ (circles) of the L308/L21 blends ($\upsilon_2 = 0.5$, 0.2, and 0.1) with the relaxation functions $\mu_{f-DTD}(t)$ (dotted curves) and $\mu_{p-DTD}(t)$ (solid curves) calculated from the dielectric data on the basis of the full-DTD and partial-DTD pictures. $\mu_{p-DTD}(t)$ coincides with $\mu_{f-DTD}(t)$ in a range of t where the solid curves are not shown.

4.2. Criterion for full-DTD. The validity of the full-DTD picture is determined according to the number $\beta_{CR}(t)$ of the entanglement segments that are CR-equilibrated in a given time scale t: The full-DTD picture should hold in a range of t where the equilibration number assumed in this picture, $\beta_{f-DTD}(t) = \{\varphi'(t)\}^{-d}$ ($d \cong 1.3$), does not exceed $\beta_{CR}(t)$, while the picture should fail at t where $\beta_{f-DTD}(t) > \beta_{CR}(t)$. We utilized this criterion to analyze the validity/failure of the DTD picture seen in Figures 5 and 6. The results are summarized below.

4.2.1. Formulation of β_{CR}. The CR-equilibration over β entanglement segments results in the stress decay by the factor of $1/\beta$. For quantitative description of this molecular scenario, we introduce *hypothetical* normalized stress decay functions $\psi_{j,CR}(t)$ (=1 at $t = 0$) of the low-M chain ($j = 1$) and high-M chain ($j = 2$) contributed *only* from the CR mechanism. This $\psi_{j,CR}(t)$ does not coincide with the measured relaxation function of a focused chain (that can relax through several mechanisms) but gives the CR-equilibration number for this chain, $\beta_{j,CR}(t) = 1/\psi_{j,CR}(t)$.

Under an assumption of the Rouse−CR dynamics,[1,3] $\psi_{j,CR}(t)$ can be written in a form,[31]

$$\psi_{j,CR}(t) = \frac{1}{N_j}\sum_{p=1}^{N_j}\exp\left(-\frac{t}{\tau_{CR,p}^{[j]}}\right) \qquad (10)$$

Here, $\tau_{CR,p}^{[j]}$ is the characteristic time for the pth CR mode of the chain j (=1 and 2) composed of N_j entanglement segments.

The values and p dependencies of $\tau_{CR,p}^{[j]}$ change according to the number of the entanglement segments included between mutual entanglement points of the high-M chains, $N_e = \upsilon_2^{-d}$ ($d \cong 1.3$). If N_j is smaller than $2N_e$, these mutual entanglements constrain the backbone of the chain j at less than two points to give no significantly effect on the CR modes of the chain j. For this case, the CR-equilibration of the chain j should be activated only by the motion of the low-M chain to have

Table 3. Parameters Determining $\tau_{CR,p}^{[j]}$ in L308/L21 Blends

	$v_2 = 0.01$	$v_2 = 0.03$	$v_2 = 0.1$	$v_2 = 0.2$	$v_2 = 0.5$
		For L21[a]			
10^2K_1/s	0.0144	0.0144	0.0144	0.0158	0.0187
		For L308[b]			
$10^2K_{2,fast}$/s	0.0144	0.0144	0.0144	0.0158	0.0187
$10^2K_{2,slow}$/s			5.61	4.79	17.7
N_2'[c]	0	0	3	8	25
N_2'' (= $N_2 - N_2'$)	62	62	59	54	37

[a] Eq 11 with $N_1 = 4$ is utilized to calculate $\tau_{CR,p}^{[1]}$ of all CR modes of L21 chain in the entire range of v_2. [b] Eqs 12 and 13 are utilized to calculate $\tau_{CR,p}^{[2]}$ of slow and fast CR modes of L308 chain at $v_2 \geq 0.1$. For $v_2 = 0.01$ and 0.03, all CR modes of this chain are classified as the fast modes and eq 13 with $N_2'' = N_2 = 62$ is utilized. [c] N_2' is evaluated as an integer closest to $N_2 v_2^d$.

a single local CR-jump frequency, and the corresponding $\tau_{CR,p}^{[j]}$ can be written in the standard Rouse−CR form,[3]

$$\tau_{CR,p}^{[j]} = K_j \sin^{-2}\left(\frac{p\pi}{2N_j}\right), \quad \text{with } p = 1, 2, .., N_j \quad (11)$$

We estimated the factor K_j from the viscoelastic CR time $\tau_{CR,G}°$ (eq 6) of the dilute L308 chain in the L21 matrix with the aid of the Rouse−CR relationship ($\tau_{CR} \propto M_1^3 M_2^2 M_e^{-3}$) by requiring that $\beta_{2,CR}(t)$ of the dilute L308 chain should increase to N_2 at $t = \tau_{CR,G}°$. Details of this estimation are described in Appendices A-1 and B, and the estimated K_j values are summarized in Table 3.

If N_j is larger than $2N_e$, the mutual entanglements of the high-*M* chains constrain the backbone of the chain *j* at two or more points to give significant entanglement effects on the CR modes of this chain; see Figure 7 where this situation is schematically depicted for the high-*M* chain ($j = 2$). In this case, the chain *j* has two local CR-jump frequencies and its CR modes should split into series of slow and fast modes activated by the motion of the high-*M* and low-*M* chains, respectively. The slow modes should emerge only after the fast CR process has erased the entanglement effect from the low-*M* chains to enlarge the effective entanglement mesh size to $a_{eff} = N_e^{1/2} a$; cf. Figure 7b. Thus, in a time scale of the slow modes, the chain *j* can be regarded to be composed of $N_j' = N_j/N_e$ enlarged segments of the size a_{eff} and entangled *only* with the high-*M* chains. Then, the chain *j* has N_j' slow CR modes and $\tau_{CR,p}^{[j]}$ of these modes can be written in the Rouse−CR form,

$$\tau_{CR,p}^{[j]} = K_{j,slow} \sin^{-2}\left(\frac{p\pi}{2N_j'}\right), \quad \text{with } p = 1, 2, ..., N_j' \text{ (for slow CR modes)} \quad (12)$$

The remaining N_j'' (= $N_j - N_j'$) fast CR modes should be essentially free from the entanglement effects from the high-*M* chains and represent the effects from the low-*M* chains. Thus, $\tau_{CR,p}^{[j]}$ of these fast modes can be modeled as those of a *dilute* chain composed of N_j'' entanglement segments and entangled with the low-*M* chains,

$$\tau_{CR,p}^{[j]} = K_{j,fast} \sin^{-2}\left(\frac{p''\pi}{2N_j''}\right), \quad \text{with } p'' = p - N_j' = 1, 2, ..., N_j'' \text{ (for fast CR modes)} \quad (13)$$

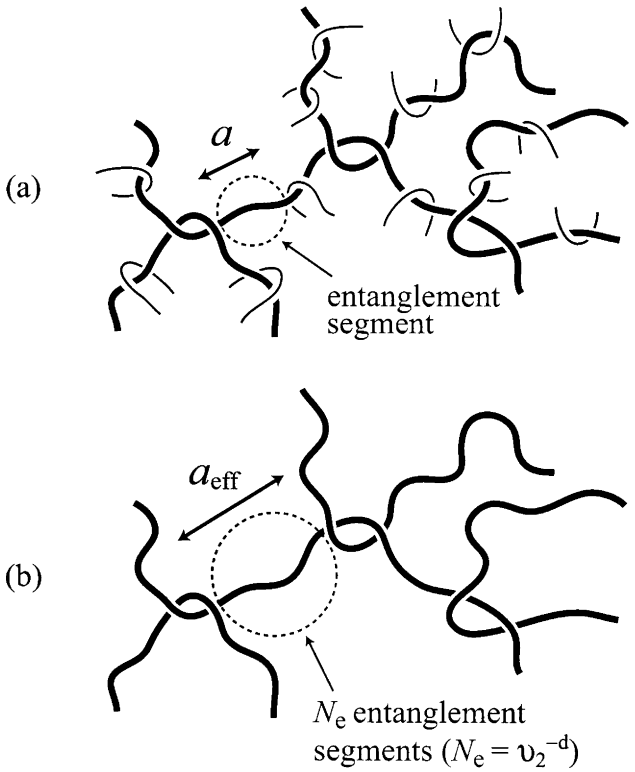

Figure 7. Schematic illustration of the blends in which the high-*M* chains (thick curves) are mutually entangled. In long time scales where the fast CR process has erased the entanglement effect from the low-*M* chains (thin curves), the blend can be regarded as a monodisperse entangled solution of the high-*M* chains having the concentration v_2. In this solution, N_e (=v_2^{-d}) entanglement segments are included between the mutual entanglement points of the high-*M* chains.

Table 4. Parameters Determining $\tau_{CR,p}^{[j]}$ in L308/L94 Blends

	$v_2 = 0.03$	$v_2 = 0.1$	$v_2 = 0.2$	$v_2 = 0.5$
		For L94[a]		
$10^2K_{1,fast}$/s	1.22	1.22	1.34	1.83
$10^2K_{1,slow}$/s			88.6	15.9
N_1'[c]	0	0	2	8
N_1'' (= $N_1 - N_1'$)	19	19	17	11
		For L308[b]		
$10^2K_{2,fast}$/s	1.22	1.22	1.34	1.83
$10^2K_{2,slow}$/s		475	72.4	17.7
N_2'[c]	0	3	8	25
N_2'' (= $N_2 - N_2'$)	62	59	54	37

[a] Eqs 12 and 13 are utilized to calculate $\tau_{CR,p}^{[1]}$ of slow and fast CR modes of L94 chain at $v_2 \geq 0.2$. For $v_2 = 0.03$ and 0.1, all CR modes of this chain are classified as the fast modes and eq 13 with and $N_1'' = N_1 = 19$ is utilized. [b] Eqs 12 and 13 are utilized to calculate $\tau_{CR,p}^{[2]}$ of slow and fast CR modes of L308 chain at $v_2 \geq 0.1$. For $v_2 = 0.03$, all CR modes of this chain are classified as the fast modes and eq 13 with $N_2'' = N_2 = 62$ is utilized. [c] N_1' and N_2' are evaluated as integers closest to $N_1 v_2^d$ and $N_2 v_2^d$, respectively.

The index *p* of these fast modes is set to run from $N_j' + 1$ to N_j in order to match the index of the slow modes ($p = 1, 2,.., N_j'$; cf. eq 12). In this model, the factor $K_{j,fast}$ is determined by the motion of the low-*M* matrix chains and thus estimated from the factor K_j for the dilute chain *j* in the same matrix (cf. eq 11). Details of this estimation are described in Appendices A-2 and B, and the estimated $K_{j,fast}$ values are summarized in Tables 3 and 4.

The factor $K_{j,slow}$ for the slow modes (eq 12) reflects the large scale CR motion of the chain *j* in the enlarged

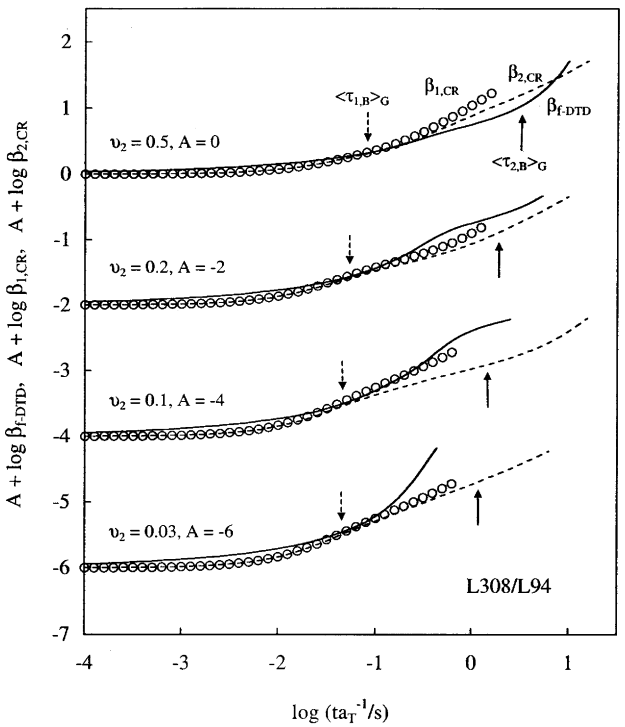

Figure 8. Comparison of the number of entanglement segments that can be equilibrated through the Rouse−CR dynamics in the L308/L94 blends, $\beta_{1,CR}$ for the low-M L94 chain (circles) and $\beta_{2,CR}$ for the high-M L308 chain (dotted curves), with the equilibration number assumed in the full-DTD picture, $\beta_{f-DTD}(t) = \{\varphi'(t)\}^{-d}$ with $d = 1.3$ (solid curves).

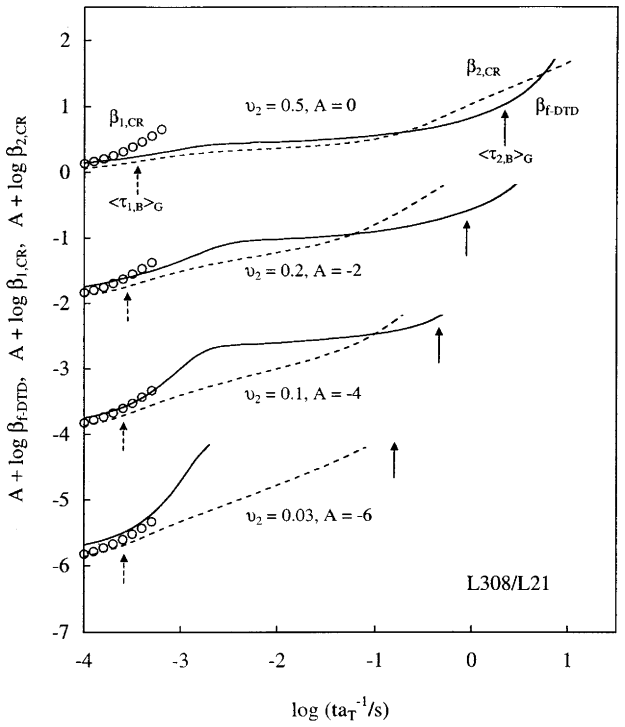

Figure 9. Comparison of the number of entanglement segments that can be equilibrated through the Rouse−CR dynamics in the L308/L21 blends, $\beta_{1,CR}$ for the low-M L21 chain (circles) and $\beta_{2,CR}$ for the high-M L308 chain (dotted curves), with the equilibration number assumed in the full-DTD picture, $\beta_{f-DTD}(t) = \{\varphi'(t)\}^{-d}$ with $d = 1.3$ (solid curves).

entanglement mesh formed only by the high-M chains. This CR motion is not affected by the fast CR process (achieving this enlargement) *if* it is slower than this process. For this case, we can estimate $K_{j,slow}$ from the K_j factor for the dilute chain j in the low-M matrix (cf. eq 11) with the aid of the Rouse−CR relationship. However, when the fast CR process is not sufficiently fast and the large scale CR motion of the chain j is affected by this process, eq 12 with this estimated $K_{j,slow}$ unreasonably gives the longest $\tau^{[j]}_{CR,1}$ that is smaller than $\tau^{[j]}_{CR,1}$° of the dilute chain j in the bulk low-M matrix (for the case of $j = 2$) or $\tau^{[j]}_{CR,1}$* in the monodisperse system (for the case of $j = 1$). Then, $K_{j,slow}$ is to be reestimated from $\tau^{[j]}_{CR,1}$° and/or $\tau^{[j]}_{CR,1}$* with the aid of the Rouse−CR relationship. Details of these estimation methods are described in Appendices A-2 and B, and the obtained $K_{j,slow}$ values are summarized in Tables 3 and 4.

4.2.2. Comparison of β_{CR} and β_{f-DTD}. From eqs 10−13 with the parameters summarized in Tables 3 and 4, we calculated the maximum number of the entanglement segments that can be CR-equilibrated in a given time scale t, $\beta_{1,CR}(t) = 1/\psi_{1,CR}(t)$ for the low-M chain and $\beta_{2,CR}(t) = 1/\psi_{2,CR}(t)$ for the high-M chain. For the L308/L94 and L308/L21 blends, respectively, Figures 8 and 9 compare $\beta_{1,CR}$ (circles) and $\beta_{2,CR}$ (dotted curves) with the equilibration number assumed in the full-DTD picture, $\beta_{f-DTD}(t) = \{\varphi'(t)\}^{-d}$ with $d = 1.3$ (solid curves). The $\beta_{j,CR}$ and β_{f-DTD} data are double-logarithmically plotted against t, and the plots are shown only in ranges of $\beta_{j,CR} < N_j$ and $\beta_{f-DTD} < N_2$ where the coarse-grained/equilibrated segment is still smaller than the chain as a whole. The arrows indicate the terminal viscoelastic relaxation times $\langle\tau_{1,B}\rangle_G$ and $\langle\tau_{2,B}\rangle_G$ of the low-M and high-M chains in the blends: $\langle\tau_{2,B}\rangle_G$ was experimentally determined with eq 4, while $\langle\tau_{1,B}\rangle_G$ was evaluated as a half the dielectric $\langle\tau_{1,B}\rangle_\epsilon$; cf. Figure 4. (Note that $\langle\tau_{1,m}\rangle_G \cong \langle\tau_{1,m}\rangle_\epsilon/2$ for the low-M chain in its monodisperse system.)

Since the *number* β is essentially an integer, a difference $|\beta_{j,CR} - \beta_{f-DTD}|$ less than unity should not be interpreted as a meaningful difference. For both L308/L21 and L308/L94 blends, $\beta_{1,CR}$ and $\beta_{2,CR}$ agree with β_{f-DTD} within this criterion (or, $\beta_{1,CR}$ is slightly larger than β_{f-DTD}) in the terminal regime of the low-M chain at $t \leq \langle\tau_{1,B}\rangle_G$; see Figures 8 and 9. Thus, for both low-M and high-M chains in this regime, the Rouse−CR equilibration actually occurs over the β_{f-DTD} segments to ensure the validity of the full-DTD picture.

As t is increased well above $\langle\tau_{1,B}\rangle_G$, the low-$M$ chain fully relaxes and the high-M chain dominates the blend behavior. In the L308/L21 and L308/L94 blends with $\upsilon_2 = 0.03$, β_{f-DTD} (solid curve) becomes larger than $\beta_{2,CR}$ (dotted curve) on this increase of t up to $\langle\tau_{2,B}\rangle_G$; see Figures 8 and 9. Namely, the Rouse−CR equilibration cannot occur over the β_{f-DTD} segments and the full-DTD picture should fail in the entire range of t well above $\langle\tau_{1,B}\rangle_G$. This failure is noted also for the L308/L94 blends with $\upsilon_2 = 0.1$ and 0.2 (cf. Figure 8).

In the L308/L21 blends with $\upsilon_2 = 0.1$ and 0.2 (Figure 9), β_{f-DTD} becomes larger than $\beta_{2,CR}$ on the increase of t to a threshold value (≅0.11 and 0.06 s for $\upsilon_2 = 0.1$ and 0.2), but a further increase of t allows β_{f-DTD} to become smaller than $\beta_{2,CR}$. Namely, in these blends, the full-DTD picture should fail at intermediate t but recover its validity in the terminal regime of the high-M chain.

For the L308/L21 blend with $\upsilon_2 = 0.5$ (Figure 9), the failure of the full-DTD picture at intermediate t is just

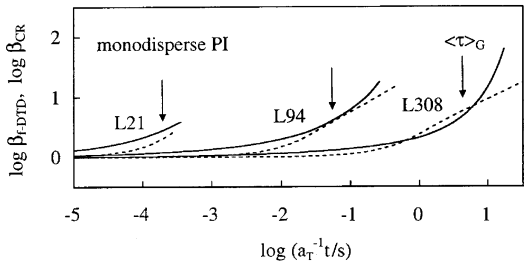

Figure 10. Comparison of the number of entanglement segments that can be equilibrated through the Rouse−CR dynamics in the monodisperse L308, L94, and L21 systems (dotted curves) with the equilibration number assumed in the full-DTD picture, $\beta_{f-DTD}(t) = \{\varphi'(t)\}^{-d}$ with $d = 1.3$ (solid curves).

mild and we may say that this picture holds approximately in the entire range of t. Similarly, the picture should be valid for the L308/L94 blend of $v_2 = 0.5$ that has $\beta_{f-DTD} \leq \beta_{2,CR}$ in the entire range of t (cf. Figure 8). This was the case also for monodisperse L308, L94, L21 systems: As shown in Figure 10, β_{CR} calculated from the parameters given in Tables 3 and 4 (dotted curves) agrees with β_{f-DTD} (solid curves) at $t < \langle\tau\rangle_G = J\eta$ within the criterion explained earlier ($|\beta_{CR} - \beta_{f-DTD}| < 1$).

All of the above results are in harmony with the results seen in Figures 5 and 6. The ranges of t where $\mu(t) > \mu_{f-DTD}(t)$ and the full-DTD picture fail coincide with the ranges of t where $\beta_{f-DTD} > \beta_{2,CR}$, confirming that the full-DTD picture is valid only when the CR-equilibration actually occurs over the $\beta_{f-DTD}(t)$ segments. (For the monodisperse systems having $\beta_{f-DTD} \cong \beta_{CR}$ at $t < \langle\tau\rangle_G$, the validity of this picture was demonstrated previously; see Figure 18 of ref 21.)

Here, we have to make a comment about the previous test[21] of the full-DTD picture for the high-M chain in the blends. In that test, we evaluated the time required for the CR-equilibration over β segments as the characteristic time of N_2/β-th Rouse−CR mode. This evaluation was based on an approximation that all higher CR modes have fully relaxed while none of the lower CR modes has relaxed when this equilibration occurs. In this paper, we have refined this approximation by introducing the hypothetical stress decay functions $\psi_{j,CR}(t)$ (eq 10) and allowing all CR modes to contribute to this equilibration to an extent determined by the mode index.

The failure of the full-DTD picture due to the insufficient CR-equilibration ($\beta_{f-DTD}(t) > \beta_{j,CR}(t)$), concluded from Figures 5, 6, 8, and 9, was also found in the previous test. However, the refinement in this paper allows us to straightforwardly evaluate $\beta_{j,CR}(t) = 1/\psi_{j,CR}(t)$ and test a molecular picture of partial-DTD. The results of this test are summarized below.

4.3. Partial-DTD Picture. 4.3.1. Partial-DTD Expression of μ. In the range of t where $\beta_{f-DTD}(t) > \beta_{j,CR}(t)$ and the full-DTD picture fails, the CR-equilibration can still occur over $\beta_{j,CR}$ entanglement segments and the tube may dilate to a diameter $a\{\beta_{j,CR}\}^{1/2}$. This molecular picture, somewhat similar to that discussed by Viovy et al.,[32] is hereafter referred to as *partial*-DTD in a sense that the dilation occurs to some part of the fully dilated $a' = a\{\varphi'(t)\}^{-d/2}$.

For this partial-DTD picture, the normalized viscoelastic relaxation function of the blend is written as

$$\mu_{p-DTD}(t) = \frac{(1 - v_2)\varphi_1'(t)}{\beta_1^*(t)} + \frac{v_2\varphi_2'(t)}{\beta_2^*(t)} \qquad (14)$$

Here, $\varphi_j'(t)$ is the survival fraction of the tube for the chain j, and $\beta_j^*(t)$ represents the actually equilibrated number of the segments of this chain

$$\beta_j^*(t) = \begin{cases} \beta_{j,CR}(t) \text{ for } \beta_{f-DTD}(t) > \beta_{j,CR}(t) \\ \beta_{f-DTD}(t) \text{ for } \beta_{f-DTD}(t) < \beta_{j,CR}(t) \end{cases} \qquad (15)$$

(This $\beta_j^*(t)$ is obtained from the $\beta_{j,CR}(t)$ and $\beta_{f-DTD}(t)$ data shown in Figures 8 and 9.)

At t where $\beta_{f-DTD}(t) \leq \beta_{j,CR}(t)$, $\varphi_j'(t)$ is dielectrically evaluated from eq 9. On the other hand, in a range of t where $\beta_{f-DTD}(t) > \beta_{j,CR}(t)$, $\varphi_j'(t)$ is evaluated after a modification of eq 9. Since the $-[\{a'(t)/a\}-1]^2/4N_j$ term in eq 9 represents the tube edge fluctuation effect on the dielectric relaxation function $\Phi_j(t)$ for an arbitrary value of the dilated diameter a', this term is to be replaced by $-[\{\beta_{j,CR}(t)\}^{1/2}-1]^2/4N_j$ for the case of $\beta_{f-DTD}(t) > \beta_{j,CR}(t)$. Namely, $\varphi_j'(t)$ is evaluated from the $\Phi_j(t)$ data on the basis of a relationship,

$$\varphi_j'(t) = \Phi_j(t) + \frac{1}{4N_j}[\{\beta_{j,CR}(t)\}^{1/2} - 1]^2 \qquad (\text{for } \beta_{j,CR} < \beta_{f-DTD}) \quad (16)$$

Equations 14−16 simply state that the concept of coarse-graining of the entanglement segments (concept of tube dilation) is valid at any t and this coarse-graining occurs to the maximum level allowed by the Rouse−CR mechanism under a given $\varphi_j'(t)$ value. Thus, $\mu_{p-DTD}(t)$ specified by eqs 14−16 reduces to $\mu_{f-DTD}(t)$ in a range of t where the full-DTD picture is valid. Note also that the partial DTD picture introduces the parameter β_j^* (eq 15) in addition to the parameters for the full-DTD picture but all parameters in eqs 14−16, including this β_j^*, are evaluated from experimental data with the method explained above.

4.3.2. Test of Partial-DTD Picture. We utilized the $\beta_{j,CR}(t)$ and $\beta_{f-DTD}(t)$ data (Figures 8 and 9) together with the $\varphi_j'(t)$ data (evaluated as above) to calculate the partial-DTD function $\mu_{p-DTD}(t)$ for the L308/L94 and L308/L21 blends with $v_2 = 0.1$, 0.2, and 0.5. In Figures 5 and 6, this $\mu_{p-DTD}(t)$ is shown with the solid curves in a range of t where the full-DTD picture fails. ($\mu_{p-DTD}(t)$ coincides with $\mu_{f-DTD}(t)$ (dotted curve) at t where the solid curves are not shown.) The calculated $\mu_{p-DTD}(t)$ is close to the $\mu(t)$ data in the entire range of t, suggesting the usefulness of the concept of the partial-DTD for these blends in which the high-M chains are mutually entangled.

Now, we focus on the L308/L94 and L308/L21 blends with $v_2 = 0.03$ in which the high-M chains are neither in the mutually entangled state ($N_2/N_e = N_2v_2^d \cong 0.65$) nor in the dilute limit (cf. Figures 3 and 4). Figure 11 compares the μ data of these blends (circles) with μ_{f-DTD} (dotted curve) and μ_{p-DTD} (solid curve) calculated from the parameters summarized in Tables 3 and 4. The μ data are much better described by the partial-DTD picture than by the full-DTD picture.

The L308/21 blend with $v_2 = 0.01$ is in the dilute limit where the high-M chains exhibit the characteristic proportionalities, $\eta_{2,B} \propto v_2$ and $J_{2,B} \propto v_2^{-1}$, and have the v_2-independent relaxation time, $\langle\tau_{2,B}\rangle_G$; see Figures 3 and 4. The Rouse−CR relaxation is observed for these

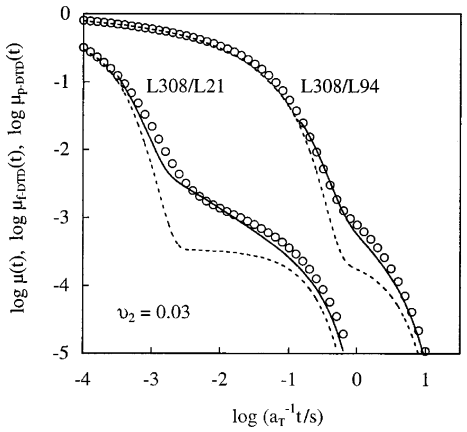

Figure 11. Comparison of the normalized viscoelastic relaxation function $\mu(t)$ (circles) of the L308/L94 and L308/L21 blends ($\upsilon_2 = 0.03$) with the relaxation functions $\mu_{f-DTD}(t)$ (dotted curves) and $\mu_{p-DTD}(t)$ (solid curves) calculated from the dielectric data on the basis of the full-DTD and partial-DTD pictures. $\mu_{p-DTD}(t)$ coincides with $\mu_{f-DTD}(t)$ in a range of t where the solid curves are not shown.

dilute high-M chains. In Figure 12, the μ data of this blend (circles) are compared with μ_{f-DTD} (dotted curve) and μ_{p-DTD} (solid curve).[33] The plus symbols indicate the relaxation function $\mu_{DTD+CR}(t)$ calculated from the Rouse−CR model for the high-M chain combined with the partial-DTD model for the low-M chain,

$$\mu_{DTD+CR}(t) = \frac{(1-\upsilon_2)\varphi_1'(t)}{\beta_1^*(t)} + \frac{\upsilon_2}{N_2}\sum_{p=1}^{N_2}\exp\left(-\frac{t}{\tau_{CR-G,p}^{[2]}}\right) \quad (17)$$

Here, β_1^* is the number of CR-equilibrated segments of the low-M chain (eq 15) evaluated from the $\varphi'(t)$ data and the parameters summarized in Table 3, and $\tau_{CR-G,p}^{[2]}$ is the viscoelastic relaxation time of the pth Rouse−CR mode of the high-M chain obtained from $\tau_{CR,G}°$ (= 0.08 s; eq 6),

$$\tau_{CR-G,p}^{[2]} = \frac{15}{\pi^2}\tau_{CR,G}°\sin^2\left(\frac{\pi}{2N_2}\right)\sin^{-2}\left(\frac{p\pi}{2N_2}\right) \quad \text{with } p = 1, 2, ..., N_2 \quad (18)$$

(The factor of $15/\pi^2$ appearing in eq 18 converts the second-moment average relaxation time $\tau_{CR,G}°$ (cf. eq 4) to the longest $\tau_{CR-G,1}^{[2]}$.)

As seen in Figure 12, the full-DTD picture (dotted curve) fails completely for the dilute high-M chain. More importantly, μ_{p-DTD} for the partial-DTD picture (solid curve) is close to the μ data (circles) and μ_{DTD+CR} (plus symbols) in the entire range of t.

All above results demonstrate the usefulness of the partial-DTD picture in a wide range of υ_2 (irrespective to the extent of the mutual entanglements of the high-M chains). Of course, this picture is not rigorous, and nonnegligible differences are observed between the μ data and μ_{p-DTD}; see Figures 5, 6, 11, and 12. Concerning this difference, we should note a conceptual limitation of the coarse-graining operation included in the partial-DTD picture: This operation smears the CR mode distribution associated with any kind of DTD process, and this smearing would be responsible (at least partly) for the observed differences. However, this limitation is not significant for large υ_2 where the coarse-grained segments remain rather small compared to the chain as a whole and the Rouse-like stress decay due to CR is fairly small in magnitude.

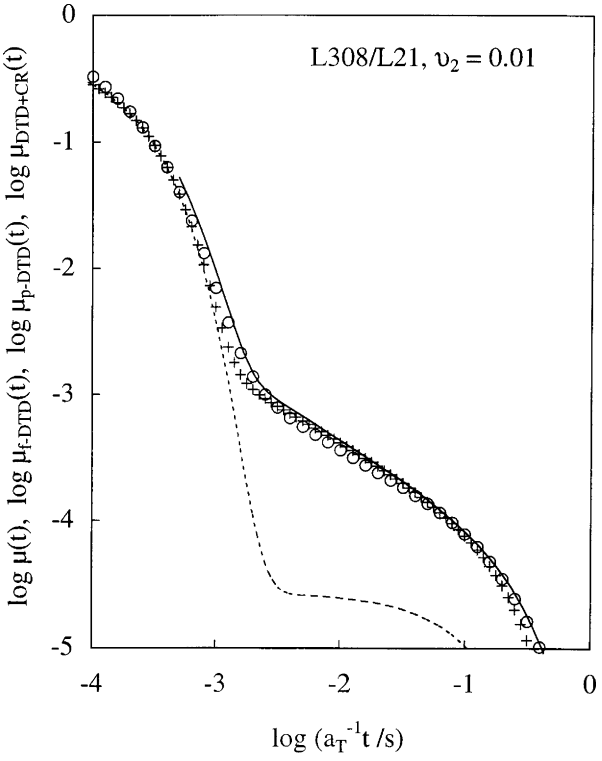

Figure 12. Comparison of the normalized viscoelastic relaxation function $\mu(t)$ (circles) of the L308/L21 blend ($\upsilon_2 = 0.01$) with the relaxation functions $\mu_{f-DTD}(t)$ (dotted curves) and $\mu_{p-DTD}(t)$ (solid curves) calculated from the dielectric data on the basis of the full-DTD and partial-DTD pictures. The plus symbols indicate $\mu_{DTD+CR}(t)$ calculated from the Rouse−CR model for the high-M chain combined with the partial-DTD model for the low-M chain.

4.4. Comments for Molecular Models. Despite the limitation explained above, the partial-DTD picture is tempting because of its simplicity and considerably good description of the dynamic data. This picture seems to serve as a useful *starting point* for refining the molecular model of the blend dynamics. Namely, we may utilize existing DTD models (such as the Milner−McLeish model[8] extended to blends by Park and Larson[11]) and leave the dilated tube diameter $a'(t)$ (or equivalent quantities such as $\beta(t) = \{a'(t)/a\}^2$) included in the model as a free parameter, instead of expressing $a'(t)$ in terms of $\varphi'(t)$. Combining this model with $a'(t)$ (or $\beta(t)$) separately calculated on the basis of the Rouse−CR dynamics, we may obtain better description of the blend dynamics. As a further refinement, the Rouse-like distribution of the CR modes is to be incorporated.[34] (DTD models available for branched chains and linear/branched blends may be refined similarly.) Formulation of these refined partial-DTD models is an interesting subject of future work. It is also important to test the refined model for various types of dynamic data such as the viscoelastic and dielectric data[1,19] as well as the dynamic scattering and NMR data,[2] because the chain motion assumed in the model is reflected differently in these data. A good example of this importance is found for the full-DTD model[7] that can excellently reproduce the viscoelastic data of star-branched chains but fails to consistently describe the dielectric data of these chains.[18] The experimental test of the partial-DTD

model formulated in the above way is the other interesting subject of future work.

5. Concluding Remarks

For the entangled PI/PI binary blends having small and large values of Struglinski−Graessley parameter, $r_{SG} = M_2M_e^2M_1^{-3} = 0.0093$ and 0.79, we have utilized the viscoelastic and dielectric data to test the validity of the full-DTD picture. For large v_2 (=0.5), this picture held satisfactorily in the entire range of t irrespective of the r_{SG} value. However, on a decrease of v_2, the picture began to fail at intermediate t (between the terminal regimes of the low-M and high-M chains) and further at long t (in the terminal regime of the high-M chains), and this failure was more significant for the blend with small r_{SG}.

The Rouse−CR analysis indicated that the failure of the full-DTD picture results from insufficient CR equilibration. Namely, in the range of t where the failure was observed, the equilibration number assumed in the full-DTD picture, $\beta_{f-DTD}(t) = \{\varphi'(t)\}^{-d}$ with $\varphi'(t)$ being the dielectrically determined tube survival fraction, was larger than the number $\beta_{CR}(t)$ allowed from the Rouse−CR dynamics.

This result led us to formulate the partial-DTD picture incorporating the maximum number β^* of the segments that can be CR-equilibrated under the given $\varphi'(t)$ value. The dynamic behavior of the blends of various v_2 was found to be well described by this picture. Although perfect description cannot be attained with the partial-DTD picture partly due to the limitation of the coarse-graining operation (smearing of the Rouse-like distribution of the CR modes), this picture is tempting because of its simplicity. The partial-DTD seems to serve as a useful starting point for refinement of the existing molecular models for various entangled systems.

Appendix A. Estimation of Front Factor for Rouse−CR Times of High-M chain

A-1. Dilute L308 Chains. For *dilute* L308 chain entangled only with the low-M chains, the CR-equilibration is activated only by the low-M chain motion and the characteristic time of the p-th Rouse−CR mode can be written as $\tau_{CR,p}^{[2]} = K_2° \sin^{-2}(p\pi/2N_2)$ with $p = 1, 2, ..., N_2$ (eq 11). The front factor $K_2°$ is determined by the motion of the matrix low-M chains.

In the L21 matrix, the Rouse−CR relaxation of the dilute L308 chain is experimentally observed and the terminal viscoelastic Rouse−CR time $\tau_{CR,G}°$ is known ($\tau_{CR,G}°$ = 0.08 s; eq 6). The front factor $K_2°$ can be determined from our molecular scenario that $\beta_{2,CR}$ (=1/$\psi_{2,CR}$) increases to N_2 (=62) and the L308 chain is globally CR-equilibrated at $t = \tau_{CR,G}°$. Thus, we utilized eq 10 to calculate $\beta_{2,CR}$ for various $K_2°$ values. It turned out that $\beta_{2,CR}$ for $K_2° = 1.44 \times 10^{-4}$ s (in L21) satisfied this scenario, as shown in Figure 13 with the solid curve.

For the dilute 308 chain, the longest characteristic time for the Rouse−CR equilibration $\tau_{CR,1}^{[2]}$ would be close to the longest dielectric relaxation time $\tau_{\epsilon,1}$ rather than the longest viscoelastic relaxation time $\tau_{G,1} = \tau_{\epsilon,1}/2$, the former directly detecting decay of the orientational memory of the chain having the type-A dipoles. For the Rouse−CR mechanism, the second-moment average viscoelastic relaxation time $\langle\tau\rangle_G$ is shorter than the longest $\tau_{G,1}$ by a factor of $\pi^2/15$. Applying this relationship to the $\tau_{CR,G}°$ data (obtained as the second-moment average relaxation time), we found $\tau_{G,1} = 0.12$ s and $\tau_{\epsilon,1} = 0.24$ s. Then, we obtained $K_2° = 1.54 \times 10^{-4}$ s by equating this $\tau_{\epsilon,1}$ to $\tau_{CR,1}^{[2]} = K_2° \sin^{-2}(\pi/2N_2)$ with $N_2 = 62$. The $\beta_{2,CR}$ calculated from this $K_2°$, shown with the dotted curve in Figure 13, is very close to the $\beta_{2,CR}$ determined under our molecular scenario (solid curve). This result lends support to the $K_2°$ value (=1.44×10^{-4} s in L21) estimated above.

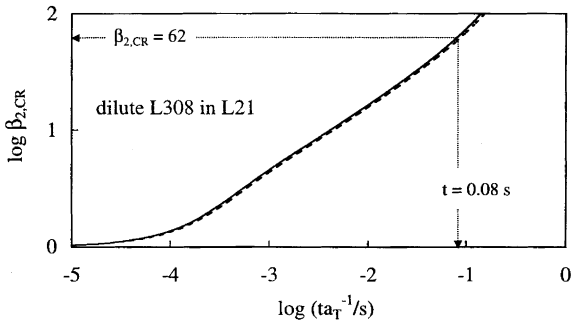

Figure 13. The number $\beta_{2,CR}$ of entanglement segments of the dilute high-M (L308) chain in the L21 matrix that can be equilibrated through the Rouse−CR mechanism. Solid curve indicates $\beta_{2,CR}$ (calculated for $K_2° = 1.44 \times 10^{-4}$ s) satisfying the molecular scenario that $\beta_{2,CR}$ increases to N_2 (=62) at $t = \tau_{CR,G}° = 0.08$ s. This $\beta_{2,CR}$ is very close to $\beta_{2,CR}$ calculated from the terminal dielectric relaxation time (dotted curve). For further details, see Appendix A-1.

For the dilute L308 chain in the L94 matrix, the terminal relaxation was not dominated by the CR mechanism and $\tau_{CR,G}°$ was not obtained experimentally. Thus, $K_2°$ cannot be estimated with the above method. However, from the Rouse−CR relationship established for the $\tau_{CR,G}°$ data of long and dilute probe chains entangled with much shorter matrix chains,[1] $\tau_{CR,G}° \propto M_1^3M_2^2M_e^{-3}$, the $K_2°$ value in the L94 matrix is estimated to be $K_2°$(in L94) = $K_2°$(in L21) × $[M_{L94}/M_{L21}]^3$ = 1.22×10^{-2} s.

A-2. Concentrated L308 Chains. The number of the (nondilated) entanglement segments included between mutual entanglement points of the high-M (L308) chains is given by $N_e = v_2^{-d}$ ($d \cong 1.3$). For $N_2 > 2N_e$, the L308 chains are entangled among themselves at more than two points (per chain) as well as with the low-M matrix chains, as schematically shown in Figure 7a. For this case, the CR-equilibration modes of a L308 chain should split into fast and slow modes activated by the motion of the low-M chains and other L308 chains, respectively.

The slow modes should emerge in a time scale where the fast CR process has erased the entanglement effects from the low-M chains. In this time scale, the L308 chain can be regarded to be composed of $N_2' = N_2/N_e$ enlarged segments and in a monodisperse solution of the concentration v_2. For the N_2' slow CR modes in this solution, the characteristic times can be written in the Rouse−CR form, $\tau_{CR,p}^{[2]} = K_{2,slow}\sin^{-2}(p\pi/2N_2')$ with $p = 1, 2, ..., N_2'$ (eq 12). The remaining N_2'' (= $N_2 - N_2'$) fast CR modes of the L308 chain should be essentially free from the entanglement effects from the other L308 chains. These fast modes can be modeled as the CR modes of a dilute chain being composed of N_2'' segments and having $\tau_{CR,p}^{[2]} = K_{2,fast} \sin^{-2}(p''\pi/2N_2'')$ with $p'' = p - N_2' = 1, 2, .., N_2''$ (eq 13).

With this modeling for the fast CR modes, the front factor $K_{2,fast}$ (eq 13) is determined by the motion of the low-M chain and thus straightforwardly estimated as

$K_{2,\mathrm{fast}} = f_r K_2°$. Here, $K_2°$ is the factor obtained for the *dilute* L308 chain (cf. Appendix A-1), and f_r represents a minor correction for the retardation of the low-M chain motion due to the concentrated L308 chains; $f_r = \langle\tau_{1,\mathrm{B}}\rangle_\epsilon / \langle\tau_{1,\mathrm{m}}\rangle_\epsilon$ with $\langle\tau_{1,\mathrm{B}}\rangle_\epsilon$ and $\langle\tau_{1,\mathrm{m}}\rangle_\epsilon$ being the dielectric relaxation times of the low-M chain in the blend and in its monodisperse system, respectively. The $K_{2,\mathrm{fast}}$ values thus estimated are summarized in Tables 3 and 4. (eq 13 with $N_2'' = N_2$ and $N_1' = 0$ is equivalent to eq 11 and applies to the L308 chains that are concentrated but not well entangled among themselves.)

Estimation of the factor $K_{2,\mathrm{slow}}$ for the slow CR modes (eq 12) requires some molecular consideration. In a case that the L308 chains have N_2' ($= N_2/N_e$) $\gg 1$ and $M_2 \gg M_1$, $\tau^{[2]}_{\mathrm{CR},p}$ of the slow modes should coincide with $\tau^{[2,\mathrm{sol}]}_{\mathrm{CR},p}$ in the monodisperse entangled solution of the L308 chains at the concentration of v_2 (in the iso-friction state) and this $\tau^{[2,\mathrm{sol}]}_{\mathrm{CR},p}$ is free from any entanglement effect from the low-M chains. Regarding this solution as a blend of a dilute L308 chain in the matrix of the other L308 chains having the concentration v_2, we may evaluate the $\tau^{[2,\mathrm{sol}]}_{\mathrm{CR},p}$ of the slowest CR mode in the solution with the aid of the Rouse−CR relationship ($\tau^{[2]}_{\mathrm{CR},1} \propto M_1{}^3 M_2{}^2 M_e{}^{-3}$; valid in bulk and solutions) as $\tau^{[2,\mathrm{sol}]}_{\mathrm{CR},p} = \{K_2° \sin^{-2}(\pi/2N_2)\}(M_2/M_1)^3 (v_2{}^d)^3$. Here, the factor $\{K_2° \sin^{-2}(\pi/2N_2)\}$ is the $\tau^{[2]}_{\mathrm{CR},1}$ of the dilute L308 chain in the bulk low-M matrix (cf. eq 11 with $K_2°$ determined in Appendix A-1), and the factor $v_2{}^d$ gives a ratio of the entanglement molecular weights in the solution and bulk low-M matrix. Utilizing this result in eq 12, we estimated $K_{2,\mathrm{slow}} = \tau^{[2,\mathrm{sol}]}_{\mathrm{CR},p} \sin^2(\pi/2N_2') = K_2° \sin^{-2}(\pi/2N_2) \sin^2(\pi/2N_2') (M_2/M_1)^3 v_2{}^{3d}$.

The above method of estimation assumes perfect coincidence of the large scale motion of the L308 chain in the solution and blend. Thus, this method fails for the cases that N_2' is not much larger than unity or M_2 is not much larger than M_1. For example, the above estimate of $K_{2,\mathrm{slow}}$ gave a value of $\tau^{[2]}_{\mathrm{CR},1} = 0.084$ s for the concentrated L308 chains ($v_2 = 0.1$) in the L21 matrix, which is *smaller* than the $\tau^{[2]}_{\mathrm{CR},1}$ value (= 0.22 s) for the *dilute* L308 chain in the same matrix. This failure reflects a situation that the fast CR process (due to the motion of the low-M chains) is not sufficiently fast and behaves as a rate-determining step for the large scale CR-motion of the L308 chain. For this case, we equated $\tau^{[2]}_{\mathrm{CR},1}$'s of the concentrated and dilute L308 chains in the same low-M matrix to reestimate $K_{2,\mathrm{slow}}$ as $K_{2,\mathrm{slow}} = K_2° \sin^{-2}(\pi/2N_2) \sin^2(\pi/2N_2')$. The $K_{2,\mathrm{slow}}$ values thus obtained are summarized in Tables 3 and 4 together with the N_2' and N_2'' values.

Appendix B. Estimation of Front Factor for Rouse−CR Times of Low-*M* Chains

The CR-equilibration modes for the low-M chains are determined according to the number of the (nondilated) entanglement segments included between mutual entanglement points of the high-M chains, $N_e = v_2{}^{-d}$ ($d \cong 1.3$). In the L308/L94 blends with $v_2 \le 0.1$ and in all L308/21 blends, $2N_e$ is larger than N_1. In these blends, the CR modes of a low-M chain should be hardly affected by the entanglements from the high-M chains (except a mild retardation effect) and have a single local CR-jump frequency. Then, the CR modes should be activated only by motion of the surrounding low-M chains and their $\tau^{[1]}_{\mathrm{CR},p}$ can be written as $\tau^{[1]}_{\mathrm{CR},p} = K_1 \sin^{-2}(p\pi/2N_1)$ with $p = 1, 2, ..., N_1$ (eq 11). The front factor K_1 is determined by the low-M chain motion and thus coincides with the factor $K_{2,\mathrm{fast}}$ for the high-M chain in the same blend (cf. Appendix A-2).

In the L308/L94 blends with $v_2 \ge 0.2$, $2N_e$ is smaller than N_1. In these blends, the CR modes of the low-M chain should be affected by high-M chains to split into the slow and fast modes having $\tau^{[1]}_{\mathrm{CR},p} = K_{1,\mathrm{slow}} \sin^{-2}(p\pi/2N_1')$ with $p = 1, 2, ..., N_1' = N_1/N_e$ (eq 12) and $\tau^{[1]}_{\mathrm{CR},p} = K_{1,\mathrm{fast}} \sin^{-2}(p''\pi/2N_1'')$ with $p'' = p - N_1' = 1, 2, ..., N_1'' = N_1 - N_1'$ (eq 13), as similar to the situation explained in Appendix A-2. Since the fast modes are modeled as the CR modes of a dilute chain composed of N_1'' entanglement segments and entangled with low-M chains, the front factor $K_{1,\mathrm{fast}}$ is determined by the motion of these low-M chains. Thus, $K_{1,\mathrm{fast}}$ coincides with $K_{2,\mathrm{fast}}$ for the high-M chain in the same blend (cf. Appendix A-2). The $K_{1,\mathrm{fast}}$ values are summarized in Tables 3 and 4.

The factor $K_{1,\mathrm{slow}}$ for the slow modes is estimated with a method similar to that explained in Appendix A-2: If the large scale CR-motion of a low-M chain in the entanglement mesh enlarged by the motion of the other low-M chains is slower than the enlarging process itself, the low-M chain can be regarded as a dilute chain that is composed of N_1' ($= N_1/N_e$) enlarged segments and entangled with the high-M chains in the monodisperse solution of the concentration v_2. With the aid of the Rouse−CR relationship, the longest CR-equilibration time of this dilute chain is evaluated to be $(M_1/M_2)^2 \tau^{[2,\mathrm{sol}]}_{\mathrm{CR},p}$ where $\tau^{[2,\mathrm{sol}]}_{\mathrm{CR},p} = \{K_2° \sin^{-2}(\pi/2N_2)\}(M_2/M_1)^3 v_2{}^{3d}$ is the longest CR time of the high-M chain in this solution (see Appendix A-2). Then, we obtain an estimate, $K_{1,\mathrm{slow}} = (M_1/M_2)^2 \tau^{[2,sol]}_{\mathrm{CR},p} \sin^2(\pi/2N_1') = \{K_2° \sin^{-2}(\pi/2N_2)\}(M_2/M_1) \sin^2(\pi/2N_1') v_2{}^{3d}$, with $K_2°$ being the front factor obtained for the dilute high-M chain in the bulk low-M matrix (cf. Appendix A-1).

This estimation is valid only when the corresponding $\tau^{[1]}_{\mathrm{CR},1}$ ($= K_{1,\mathrm{slow}} \sin^{-2}(\pi/2N_1')$) is longer than the longest CR time in the bulk monodisperse system of the low-M chains, $\tau^{[1]}_{\mathrm{CR},1}{}^* = (M_1/M_2)^2\{K_2° \sin^{-2}(\pi/2N_2)\}$ with the factor $\{K_2° \sin^{-2}(\pi/2N_2)\}$ being the longest CR time of the dilute high-M chain in the bulk matrix of low-M chain (cf. Appendix A-1). For the L308/L94 blends, this validity was found for $v_2 = 0.5$ but not for $v_2 = 0.2$. Thus, $K_{1,\mathrm{slow}}$ for $v_2 = 0.2$ was reestimated from this $\tau^{[1]}_{\mathrm{CR},1}{}^*$ as $K_{1,\mathrm{slow}} = \tau^{[1]}_{\mathrm{CR},1}{}^* \sin^2(\pi/2N_1')$. The $K_{1,\mathrm{slow}}$ values estimated in this way are summarized in Tables 3 and 4 together with the N_1' and N_1'' values.

References and Notes

(1) Watanabe, H. *Prog. Polym. Sci.* **1999**, *24*, 1253.
(2) McLeish, T. C. B. *Adv. Phys.* **2002**, *51*, 1379.
(3) Graessley, W. W. *Adv. Polym. Sci.* **1982**, *47*, 67.
(4) Likthman, A. E.; McLeish, T. C. B. *Macromolecules* **2002**, *36*, 6332.
(5) Marrucci, G. *J. Polym. Sci. Polym. Phys. Ed.* **1985**, *23*, 159.
(6) Ball, R. C.; McLeish, T. C. B. *Macromolecules* **1989**, *22*, 1911.
(7) Milner, S. T.; McLeish, T. C. B. *Macromolecules* **1997**, *30*, 2159; **1998**, *31*, 7479.
(8) Milner, S. T.; McLeish, T. C. B. *Phys. Rev. Lett.* **1998**, *81*, 725.
(9) Colby, R. H.; Rubinstein, M. *Macromolecules* **1990**, *23*, 2753.
(10) Milner, S. T.; McLeish, T. C. B.; Young, R. N.; Hakiki, A.; Johnson, J. M. *Macromolecules* **1998**, *31*, 9345.
(11) Park, S. J.; Larson, R. G. *Macromolecules* **2004**, *27*, 597.

(12) Tsenoglou, C. *Polym. Prepr. (ACS, Div. Polym. Chem.)* **1987**, *28*, 185; *Macromolecules* **1991**, *24*, 1762.
(13) Tuminello, W. H. *Polym. Eng. Sci.* **1986**, *26*, 1339.
(14) des Cloizeaux, J. *Macromolecules* **1990**, *23*, 3992.
(15) Matsumiya, Y.; Watanabe, H.; Osaki, K. *Macromolecules* **2000**, *33*, 499.
(16) Watanabe, H.; Matsumiya, Y.; Osaki, K. *J. Polym. Sci., Part B: Polym. Phys.* **2000**, *38*, 1024.
(17) Matsumiya, Y.; Watanabe, H. *Macromolecules* **2001**, *34*, 5702.
(18) Watanabe, H.; Matsumiya, Y.; Inoue, T. *Macromolecules* **2002**, *35*, 2339.
(19) Watanabe, H. *Macromol. Rapid Commun.* **2001**, *22*, 127.
(20) Watanabe, H. *Kor.-Austr. Rheol. J.* **2001**, *13*, 205.
(21) Watanabe, H.; Ishida, S.; Matsumiya, Y.; Inoue, T. *Macromolecules* **2004**, *37*, 1937.
(22) Struglinski, M. J.; Graessley, W. W. *Macromolecules* **1985**, *18*, 2630.
(23) Riande, E.; Saiz, E. *Dipole Moments and Birefringence of Polymers*; Prentice Hall: Englewood Cliffs, NJ, 1992.
(24) Watanabe, H.; Yamazaki, M.; Yoshida, H.; Kotaka, T. *Macromolecules* **1991**, *24*, 5573.
(25) Yoshida, H.; Watanabe, H.; Kotaka, T. *Macromolecules* **1991**, *24*, 572.
(26) Watanabe, H.; Sakamoto, T.; Kotaka, T. *Macromolecules* **1985**, *18*, 1436.
(27) The second-moment average relaxation time $\langle\tau_{2,B}\rangle_G$ (eq 4) is expressed in terms of the viscoelastic relaxation spectrum $H_{2,B}(\tau)$ of the high-M chains in the blends as[1, 26] $\langle\tau_{2,B}\rangle_G = [\int_{-\infty}^{\infty} H_{2,B}(\tau)\,\tau^2\,d(\ln\tau)]/[\int_{-\infty}^{\infty} H_{2,B}(\tau)\,\tau\,d(\ln\tau)]$. This $\langle\tau_{2,B}\rangle_G$ is an average heavily weighing on slow modes and close to the longest viscoelastic relaxation time $\tau_{G,1}$. Specifically, $\langle\tau_{2,B}\rangle_G = (\pi^2/15)\tau_{G,1}$ for the Rouse−CR mechanism.[1,]
(28) (a) A modified Rouse−CR relationship proposed by Montfort et al.,[28b] $\tau_{CR}^{\circ} \propto M_1^{2.3\pm0.1} M_2^{1.9\pm0.1}$ (for constant M_e), was also utilized to estimate $\tau_{CR,G}^{\circ}$ of L308 in the L94 matrix from the $\tau_{CR,G}^{\circ}$ data in the L21 matrix. The $\langle\tau_{2,B}\rangle_G$ data in the L94 matrix were smaller than this estimate, and the suppression of the CR-equilibration in L94 was concluded also with this modified relationship. However, we should emphasize that the data[28b] utilized to deduce the modified relationship were *not* obtained in the dilute regime (where the proportionalities $\eta_{2,B} \propto v_2$ and $J_{2,B} \propto v_2^{-1}$ should be observed) and the validity of this relationship for dilute probe chains has been questioned; see ref 1 for further explanation. For this reason, this paper utilizes the nonmodified Rouse−CR relationship to confirm the suppression of the CR-equilibration in the L94 matrix. (b) Montfort, J. P.; Marin, G.; Monge, P. *Macromolecules* **1984**, *17*, 1551.
(29) Colby, R. H.; Rubinstein, M. *Macromolecules* **1990**, *23*, 2753.
(30) Park, S.; Larson, R. G. *J. Rheol.* **2003**, *47*, 199.
(31) In the Rouse−CR expression of the hypothetical stress decay function (eq 10), we have neglected a difference between the number of entanglement segments N_j and the number of the entanglement bond vectors $N_j - 1$. For the L308 and L94 chains having large N_j value (= 62 and 19), this does not raise any significant problem. In addition, this difference itself is a delicate issue related to the boundary condition for the Rouse−CR equation of motion. (This condition changes according to a treatment of the segments at the chain ends.).
(32) Viovy, J. L.; Rubinstein, M.; Colby, R. H. *Macromolecules* **1991**, *24*, 3587.
(33) The $\varphi_j'(t)$ of the low-M and high-M chains in the L308/L21 blends with $v_2 = 0.01$, utilized in Figure 12, were evaluated from the dielectric data[21] of the blends with $v_2 = 0.02$ and 0.03 after short extrapolation.
(34) (a) Dielectric studies of dipole-inverted PI chains revealed that dilute probe chains in the CR regime have nonsinusoidal eigenfunctions although these eigenfunctions and the accompanying relaxation times give the viscoelastic relaxation functions close to the Rouse function.[19,34b,34c] This experimental fact indicates that the actual CR motion of these chains is not perfectly described by the Rouse−CR dynamics. This non-Rouse feature of the CR mechanism is to be also incorporated in the highly refined partial-DTD model. (b) Watanabe, H.; Urakawa, O.; Kotaka, T. *Macromolecules* **1994**, *27*, 3525. (c) Watanabe, H.; Matsumiya, Y.; Osaki, K.; Yao, M.-L. *Macromolecules* **1998**, *31*, 7538.

MA0495689